

NON-INTRUSIVE SENSING IN TURBULENT BOUNDARY LAYERS VIA DEEP FULLY-CONVOLUTIONAL NEURAL NETWORKS

Luca Guastoni

FLOW, KTH Engineering Mechanics,
Swedish e-Science Research Centre (SeRC)
SE-100 44 Stockholm, Sweden
guastoni@mech.kth.se

Arivazhagan G. Balasubramanian

FLOW, KTH Engineering Mechanics,
SE-100 44 Stockholm, Sweden
argb@kth.se

Alejandro Güemes

Aerospace Engineering Research Group
Universidad Carlos III de Madrid
28911, Leganés, Spain
aguemes@ing.uc3m.es

Andrea Ianiro

Aerospace Engineering Research Group
Universidad Carlos III de Madrid
28911, Leganés, Spain
aianiro@ing.uc3m.es

Stefano Discetti

Aerospace Engineering Research Group
Universidad Carlos III de Madrid
28911, Leganés, Spain
sdiscett@ing.uc3m.es

Philipp Schlatter

FLOW, KTH Engineering Mechanics,
Swedish e-Science Research Centre (SeRC)
SE-100 44 Stockholm, Sweden
pschlatt@mech.kth.se

Hossein Azizpour

School Elect. Eng. and Comp. Sci., KTH
Swedish e-Science Research Centre (SeRC)
SE-100 44 Stockholm, Sweden
azizpour@kth.se

Ricardo Vinuesa

FLOW, KTH Engineering Mechanics,
Swedish e-Science Research Centre (SeRC)
SE-100 44 Stockholm, Sweden
rvinuesa@mech.kth.se

ABSTRACT

Flow-control techniques are extensively studied in fluid mechanics, as a means to reduce energy losses related to friction, both in fully-developed and spatially-developing flows. These techniques typically rely on closed-loop control systems that require an accurate representation of the state of the flow to compute the actuation. Such representation is generally difficult to obtain without perturbing the flow. For this reason, in this work we propose a fully-convolutional neural-network (FCN) model trained on direct-numerical-simulation (DNS) data to predict the instantaneous state of the flow at different wall-normal locations using quantities measured at the wall. Our model can take as input the heat-flux field at the wall from a passive scalar with Prandtl number $Pr = \nu/\alpha = 6$ (where ν is the kinematic viscosity and α is the thermal diffusivity of the scalar quantity). The heat flux can be accurately measured also in experimental settings, paving the way for the implementation of a *non-intrusive* sensing of the flow in practical applications.

INTRODUCTION

One of the possible applications of active flow control in wall-bounded flows is to reduce the skin friction. The control

can be designed either as an open-loop or closed-loop system. In the first case, no information is obtained from the flow with measurements. This means that the control is prescribed independently from the current flow state. It can be a force, introduced with a periodic motion (Quadrio *et al.*, 2009) or a deformation (Tomiya & Fukagata, 2013) of the wall, or it can be obtained through blowing and suction at the wall (Fahland *et al.*, 2021). In the closed-loop case, the drag is reduced by modifying the velocity near the wall according to the changes of the velocity within the flow field (Choi *et al.*, 1994). It is highly desirable to monitor the flow with non-intrusive measurements. Hence, sensors are typically located at the wall in practical applications. One of the downsides of this approach is a poor reconstruction of the flow farther from the wall, a fact that hinders the possibility to design an accurate control for coherent structures in that flow region. This highlights the need of a reliable estimation of the flow field that can be performed, for instance, using extended proper orthogonal decomposition (EPOD, Borée, 2003), which is equivalent to linear stochastic estimation (LSE, Encinar & Jiménez, 2019), or transfer functions (Sasaki *et al.*, 2019). Recently, neural-network models have shown excellent results in monitoring the instantaneous state of the flow using quantities measured at the wall in numerical simulations. For instance, convolu-

tional neural networks (CNNs) have been used to correlate the two wall-shear-stress components to the instantaneous wall-normal heat flux (Kim & Lee, 2020). In that case both the measurements and the predictions are at the same location, *i.e.* at the wall. In this work, on the other hand, we consider input measurements at the wall and target flow-state estimation above the wall. The chosen network architecture is a fully-convolutional network (FCN), conceptually similar to the one proposed by Guastoni *et al.* (2021). However, other architectures have been tested in the literature for the same task, *e.g.* super-resolution generative adversarial networks (SR-GANs, Güemes *et al.*, 2021). Despite machine-learning-based control has been tested in experimental settings with promising results (Gautier *et al.*, 2015), it is difficult to acquire from experimental facilities the large datasets that are needed to train neural networks models. For this reason, in this study we perform the training of the networks using the data obtained from numerical flow simulations. Furthermore, the networks are trained to predict the flow using measurements that can be obtained in experiments. Thanks to this choice, the trained network models will be able to be fine-tuned on the experimental data once they are available. In future studies, we will use the methods developed here in the water tunnel facility of Universidad Carlos III de Madrid coupling time-resolved IR thermography (Raiola *et al.*, 2017) with tomographic Particle Image Velocimetry (Discetti & Coletti, 2018), to assess the feasibility of deploying this prediction framework in a practical application.

DATASET

The direct numerical simulation (DNS) from which the measurements and the target output fields are sampled is performed using the pseudo-spectral code SIMSON (Chevalier *et al.*, 2007). While our previous work (Guastoni *et al.*, 2021) focused on a fully-developed flow, namely a turbulent open channel flow, in this work we simulate a zero-pressure-gradient (ZPG) turbulent boundary layer (TBL). The inflow condition for the velocity is a laminar profile. A random trip forcing is applied to trigger the transition to a turbulent boundary layer. A fringe forcing is applied at the outflow in order to achieve periodicity at the boundary, as requested by the solution method. A passive scalar θ representing the temperature of the fluid is also simulated. We consider Prandtl number $Pr = 6$ and impose an isothermal wall boundary condition $\theta|_{y=0} = 0$.

The choice of a spatially-developing flow implies an additional degree of complexity in the predictions with respect to the previously-studied channel flow, since the friction Reynolds number Re_τ (based on the boundary-layer thickness and the friction velocity $u_\tau = \sqrt{\tau_w/\rho}$, where τ_w is the wall-shear stress and ρ is the fluid density) increases with the streamwise location x within the sampled fields. The highest considered Re_τ is 396, which is similar to the maximum value we expect to sample in our experimental setting. We sample the wall-shear-stress components, as well as the wall pressure. Note that we considered a reference friction velocity at the middle of the computational domain, which implies that the actual inner-scaled location that is actually sampled slightly varies along the streamwise direction. However, the variation is within $\pm 0.1y^+$. Furthermore, the flux of a passive scalar $\partial\theta/\partial y$ is sampled at the wall. The velocity-fluctuation fields (whose streamwise, wall-normal and spanwise components are denoted u , v and w , respectively) are sampled at four wall-normal locations: $y^+ = 15, 30, 50$ and 100 . Here the ‘+’

denotes viscous scaling, *i.e.* in terms of the friction velocity u_τ or the viscous length $\ell^* = \nu/u_\tau$ (where ν is the fluid kinematic viscosity).

Note that the sampled fields include both the initial, transitional part of the flow and the final region affected by the fringe forcing. On the other hand, the neural-network models predict only a portion of the field. Depending on the size, we can identify two different types of samples, as shown in figure 1: *full domain* (FD) samples have streamwise and spanwise lengths of $x_s/\delta_0^* = 600$ and $z_s/\delta_0^* = 50$, respectively. Here δ_0^* is the displacement thickness of the laminar boundary layer at the inflow. The samples do not include the initial ($x/\delta_0^* < 200$) and the final region ($800 < x/\delta_0^* < 1000$). When the streamwise length of the samples is reduced to $x_s/\delta_0^* = 300$, we refer to them as *half-domain* (HD) samples. The grid points considered in the FD case are $N_{x,s} \times N_{z,s} = 1960 \times 320$, while for HD they are 980×320 .

In order to obtain a sufficiently large number of fields, five different realizations of the simulation are performed using five different trip-forcing random seeds. The *training dataset* includes 7,474 samples obtained from three of the five simulations. The *validation dataset* consists of 2,195 samples, taken from a separate DNS to avoid unwanted correlations with the training dataset. The *test dataset* is obtained from the remaining simulation, it includes 1,973 samples and the overall sampled time for testing is sufficient to obtain converged turbulence statistics.

NEURAL-NETWORK MODEL

In this work, we consider several network architectures for different types of predictions. Based on the quantities sampled at the wall that are provided as input to the neural network, three types of predictions are investigated, as summarized in table 1.

Table 1. Summary of inputs and outputs for different prediction types. The inputs are measured at the wall, the outputs are sampled at a given wall-normal location.

Type	Inputs	Outputs
I	$\partial u/\partial y, \partial w/\partial y, p$	u, v, w
II	$\partial \theta/\partial y, \partial w/\partial y, p$	u, v, w
III	$\partial \theta/\partial y$	u, v, w

In the first problem, a neural-network model is trained to predict the velocity-fluctuation fields farther from the wall using the streamwise and spanwise wall-shear-stress components, as well as the wall-pressure fields. The predictions of the first problem are denoted as *type I*. These predictions use the same inputs and outputs as those of our previous work (Guastoni *et al.*, 2021). In the second problem the streamwise wall-shear stress is substituted with the heat flux field corresponding to the passive scalar at $Pr = 6$. We refer to these predictions as *type-II* predictions. Finally, a third problem is considered, using only the heat-flux field at $Pr = 6$ as input (*type III*). The latter type aims to reproduce our experimental setting, in which we will be able to measure only the wall heat-flux field.

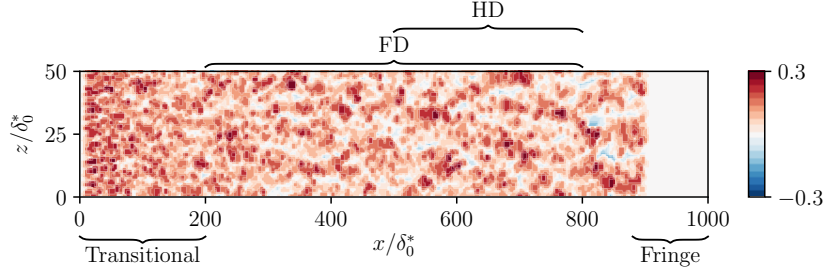


Figure 1. Representation of full domain (FD) and half domain (HD) in a sampled streamwise velocity-fluctuation field at $y^+ = 30$.

All the trained models are fully-convolutional neural networks, meaning that the input information is processed by a sequence of convolutional layers, but there are no fully-connected layers at the end, as it happens for convolutional neural networks, that are typically employed for classification tasks on the entire input. The inputs of the FCN model are normalized with the mean and standard deviation computed on the training samples. The velocity-fluctuation fields predicted by the FCN are scaled with the ratio of the corresponding root-mean-squared (RMS) values and the streamwise RMS value, following Guastoni *et al.* (2021). The scaled output quantities are indicated with $\hat{\bullet}$.

FCNs allow an accurate reconstruction of the flow fields thanks to their capability to identify simple features and to combine them into progressively more complex ones. The FCN used as reference (Guastoni *et al.*, 2021) is relatively shallow (*i.e.* few convolutional layers), with a high number of kernels per layer. On the other hand, the network architectures tested in this work have a higher number of layers with fewer kernels per layer. These modifications are designed to enhance the compositional capabilities of the model without increasing its GPU-memory footprint and computational-training cost. Note that the output of each convolutional layer is slightly smaller than the input, depending on the size of the convolutional kernel (Dumoulin & Visin, 2016). When a very high number of layers is used, the output can become significantly smaller than the input. In our work, the size of the output is kept constant by modifying the size of the input field according to the architecture. This is realized by sampling a larger area in the streamwise direction and by padding periodically the field in the spanwise direction. Different models with a varying number of layers and trainable parameters are trained in order to identify the best combination of these network architecture parameters. Such comparison is performed on *type-III* predictions at $y^+ = 30$, in an effort to optimize the network performance for its experimental use. The FCN is trained using the Adam (Kingma & Ba, 2015) stochastic algorithm to minimize the mean-squared error (MSE) of the predictions with respect to the turbulent fields sampled from the DNS:

$$\mathcal{L}(\hat{\mathbf{u}}_{\text{FCN}}; \hat{\mathbf{u}}_{\text{DNS}}) = \frac{\sum_{i=1}^{N_{x,s}} \sum_{j=1}^{N_{z,s}} |\hat{\mathbf{u}}_{\text{FCN}}(i, j) - \hat{\mathbf{u}}_{\text{DNS}}(i, j)|^2}{N_{x,s} N_{z,s}}, \quad (1)$$

where boldface indicates the vectors containing the three velocity components and $|\bullet|$ represents the L_2 norm. We refer to the error in the individual components using $\mathcal{L}(\bullet)$ for brevity. For *type-III* predictions, an additional auxiliary loss function is also considered: streamwise, spanwise wall-shear stress and wall-pressure field are predicted by the network as

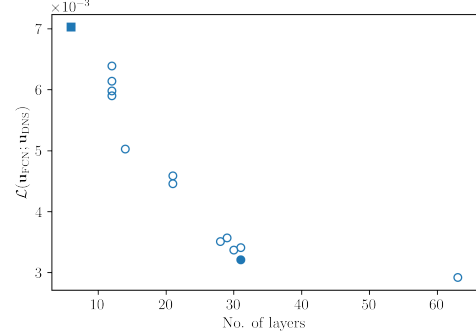


Figure 2. MSE in the predictions as a function of the number of layers of the network for *type-III* predictions. The filled square marker represents the network model used in Guastoni *et al.* (2021), while the filled circle is the model proposed in this work. These two latter models are compared in all the subsequent analysis.

an intermediate output, in an effort to drive the internal flow representation of the FCN towards physically-meaningful and interpretable quantities.

RESULTS AND DISCUSSION

The quality of the network predictions is assessed using the MSE with respect to the corresponding DNS fields and the turbulence statistics accuracy. The pre-multiplied two-dimensional power-spectral densities are also computed, to assess the amount of energy reconstructed for the different scales. The comparison of the different network architectures is based on the MSE because it is the metric used to optimize the network performance during training. While increasing the number of trainable parameters in the network does not have a clear effect on the MSE, figure 2 highlights the correlation between the number layers and the network performance for *type-III* predictions. The higher the number of layers, the lower the corresponding mean-squared error in the predictions.

The network architecture trained in Guastoni *et al.* (2021) and the deepest network in this work have roughly the same number of trainable parameters, however the latter network shows a prediction error that is about 50% lower than the former. This result suggests a higher importance of the compositional capabilities of the network over its capacity. Despite achieving the best performance in the comparison, our deepest network was not selected for the subsequent analysis primarily because of the low ratio between the output and input field size. In particular, in an experimental setting, we would

not be able to increase the size of the input fields as done in this numerical investigation, hence a deeper network would inevitably result in a smaller output field in which fewer turbulent features are represented. In the remaining of this work, we present the results obtained with the second best architecture, which has about half of the layers than our deepest one, allowing to maintain a more acceptable output/input size ratio, while providing a comparable performance in terms of MSE. Note that this network has a higher number of trainable parameters, having a higher number of kernels per layer than the deepest network trained.

Given the network architecture, the predictions on the full-domain and on the half-domain datasets are compared. One of the advantages of the FCN is that the architecture does not depend on the size of the input. Either datasets can then be used to train the neural-network model. Despite providing more information per sample during training, the predictions of the model optimized on the full-domain dataset are less accurate than the ones on the half-domain dataset. This can be explained by considering that the boundary layer is a spatially-developing flow. This means that each sample contain a range of Reynolds numbers that need to be predicted. The smaller the range, the more accurate the predictions. This result is encouraging for the future experimental applications, since the input data that can be obtained are limited to a small interrogation window (*e.g.* obtained from particle-image velocimetry), with a small Reynolds-number range. Because of these observations, the prediction results in the subsequent part of the paper will be only related to the half-domain dataset.

Once the network architecture and the dataset are chosen, the model is trained three times with different random initialization in order to verify the consistency of the stochastic optimizations. The reported results show the average performance of the three models. When three inputs are considered (*type-I* and *type-II* predictions), the present network is able to reconstruct the non-linear relation between input and output fields with a higher accuracy than the FCN proposed in Guastoni *et al.* (2021), as shown in figure 3 (*type-I* predictions). The improvement is consistent across the entire range of investigated wall-normal locations. On the other hand, the performance degrades in a similar way as we move farther away from the wall. The accuracy of the present network at $y^+ = 50$ is comparable to that of the FCN in Guastoni *et al.* (2021) at $y^+ = 30$. At $y^+ = 100$, the MSE in the wall-normal and spanwise directions is similar for both architectures. The accuracy improvement is even more pronounced when considering the predicted turbulent statistics. In short, the error is lower at all y^+ locations and even at $y^+ = 100$, the current FCN performs substantially better than its predecessor.

Type-II predictions represent an intermediate step towards the flow estimation using only the heat flux. When passing from *type I* to *type II*, the error is higher for all the velocity components, however the streamwise component is the most affected, as the heat flux at the wall is less correlated to the velocity-fluctuations away from the wall than the streamwise wall-shear stress. The percentual increment of the MSE due to the added difficulty of the predictions is similar for both networks, note however that the predictions from the FCN proposed in this study were significantly more accurate than the FCN in Guastoni *et al.* (2021). For this reason, the current FCN is found to perform better across the entire range of wall-normal locations, even for *type-II* predictions.

Type-III predictions are performed at two wall-normal distances: $y^+ = 15$ and 30. The resulting MSE is about three times higher when compared to *type-II* predictions, indicat-

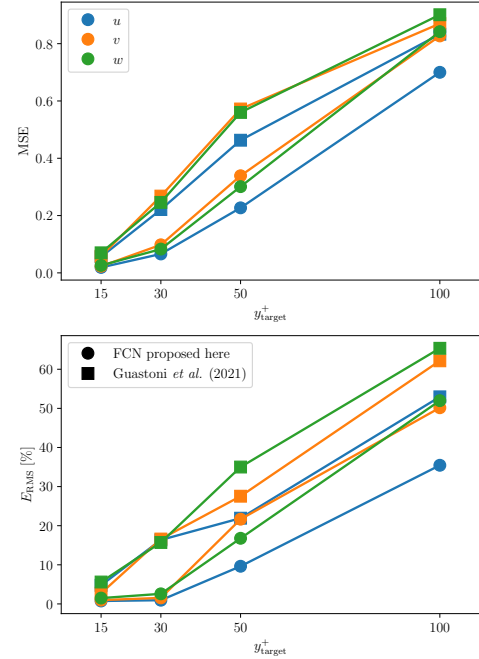


Figure 3. MSE (top) and turbulence-statistics error (bottom) obtained in *type-I* predictions with respect to target fields at different wall-normal locations. The error for each velocity component is normalized with the square of the corresponding fluctuations intensity.

ing that information in the spanwise wall-shear stress and wall pressure has an important role in the reconstruction of the fields away from the wall. Note that making the use of a deeper FCN necessary to achieve satisfactory predictions of this type, as shown by the error comparison with Guastoni *et al.* (2021) in table 2. With the use of the auxiliary loss the MSE is only

Table 2. Error comparison in *Type-III* predictions at $y^+ = 30$ using the network model from Guastoni *et al.* (2021) and the one proposed here. The variance of the statistical error is computed across the different training runs.

	Guastoni <i>et al.</i>	Current FCN
$\mathcal{L}(u)/u_{\text{RMS}}^2$	0.592	0.271
$\mathcal{L}(v)/v_{\text{RMS}}^2$	0.638	0.335
$\mathcal{L}(w)/w_{\text{RMS}}^2$	0.850	0.330
$E_{\text{RMS}}(u)$ [%]	36.82 ± 0.67	11.87 ± 0.49
$E_{\text{RMS}}(v)$ [%]	39.48 ± 0.92	14.14 ± 0.93
$E_{\text{RMS}}(w)$ [%]	57.26 ± 1.24	14.04 ± 0.74

about 5% lower, while the predicted turbulence statistics are 20% better than when the auxiliary loss function is not used. A sample *type-III* prediction at $y^+ = 30$ using the auxiliary loss function is shown in figure 4. From this figure, it is possible to observe that the FCN is able to reconstruct the large-scale features of the flow in all three velocity components starting from the heat-flux field only. The smaller-features reconstruc-

tion is less accurate, in particular the maximum positive and negative fluctuations are typically underestimated. This is related to the use of the mean-squared error as loss function for the optimization.

A more comprehensive overview of the predicted energy at the different scales is provided by the spectra, shown in figure 5. We compare the spectra of *type-II* and *type-III* predictions at $y^+ = 30$. The amount of reconstructed energy is lower in *type-III* predictions than in *type-II*. Furthermore, it is possible to observe that eliminating the spanwise wall-shear stress and wall pressure has a higher impact on the prediction of the shorter wavelengths, both in the streamwise and spanwise direction. The accuracy reduction is more evident in the pre-multiplied wall-normal and spanwise spectra. This is expected, as the wall-pressure is well correlated with the wall-normal component of the velocity and the spanwise wall-shear stress helps to improve the prediction of the corresponding velocity-fluctuation component.

CONCLUSIONS

In this work, we assessed the prediction capabilities of a fully-convolutional network (FCN) using DNS data sampled from a turbulent boundary layer flow, with a maximum Reynolds number of $Re_\tau = 396$. We optimize the architecture of the FCN in order to minimize the MSE in the predictions, while maintaining a satisfactory output/input ratio of the field size. The resulting network yields *type-III* predictions at $y^+ = 30$ with an error that is 50% lower than that of the previously-studied architectures (Guastoni *et al.*, 2021). A higher number of layers determines a larger receptive field for the network, and it enhances its compositional capabilities. The prediction accuracy is proven to be more sensitive to this parameter than the network capacity (*i.e.* the number of trainable parameters). The use of alternative, yet similar network architectures (*e.g.* ResNet by He *et al.* (2016) or UNet by Ronneberger *et al.* (2015)) was only partially explored and for this reason not reported, preventing a more comprehensive analysis of the available network architectures. The use of skip connections, present in the aforementioned architectures, can potentially improve the network performance further, but this assessment is left for future work. The architectural improvements described here are essential to achieve a satisfactory velocity field reconstruction, given the additional difficulties related to the choice of a spatially-evolving flow, and the use to input quantities that are less informative than the ones used in the previous studies.

After assessing the prediction capabilities of the FCN using DNS data, future work will be devoted to testing the neural-network model in an experimental setting. In this case, the resolution of the measured quantities is typically lower than that of DNS samples. To address this issue, the FCN model should be first trained using DNS data aptly modified to mimic experimental data and then using samples taken directly from a wind tunnel. Testing the trained networks on this synthetic experimental data represents the next step towards the network model deployment in an experiment.

ACKNOWLEDGEMENTS

The authors acknowledge the funding provided by the Swedish e-Science Research Centre (SeRC), the G. Gustafsson Foundation and the Knut and Alice Wallenberg (KAW) Foundation. The numerical simulations were carried out on resources provided by the Swedish National Infrastruc-

ture for Computing (SNIC) at PDC. S.D. and A.I were partially supported by the project ARTURO, ref. PID2019-109717RB-I00/AEI/10.13039/501100011033, funded by the Spanish State Research Agency.

REFERENCES

- Borée, J. 2003 Extended proper orthogonal decomposition: a tool to analyse correlated events in turbulent flows. *Exp. Fluids* **35** (2), 188–192.
- Chevalier, M., Schlatter, P., Lundbladh, A. & Henningson, D. S. 2007 SIMSON : a pseudo-spectral solver for incompressible boundary layer flows. *Tech. Rep.* KTH Royal Institute of Technology, Stockholm.
- Choi, H., Moin, P. & Kim, J. 1994 Active turbulence control for drag reduction in wall-bounded flows. *J. Fluid Mech.* **262**, 75–110.
- Discetti, S. & Coletti, F. 2018 Volumetric velocimetry for fluid flows. *Meas. Sci. Technol.* **29** (4), 042001.
- Dumoulin, V. & Visin, F. 2016 A guide to convolution arithmetic for deep learning. *Preprint arXiv:1603.07285*.
- Encinar, M. P. & Jiménez, J. 2019 Logarithmic-layer turbulence: A view from the wall. *Phys. Rev. Fluids* **4**, 114603.
- Fahland, G., Stroh, A., Frohnappfel, B., Atzori, M., Vinuesa, R., Schlatter, P. & Gatti, D. 2021 Investigation of blowing and suction for turbulent flow control on airfoils. *AIAA J.* **59** (11), 4422–4436.
- Gautier, N., Aider, J.-L., Duriez, T., Noack, B. R., Segond, M. & Abel, M. 2015 Closed-loop separation control using machine learning. *J. Fluid Mech.* **770**, 442–457.
- Guastoni, L., Güemes, A., Ianiro, A., Discetti, S., Schlatter, P., Azizpour, H. & Vinuesa, R. 2021 Convolutional-network models to predict wall-bounded turbulence from wall quantities. *J. Fluid Mech.* **928**, A27.
- Güemes, A., Discetti, S., Ianiro, A., Sirmacek, B., Azizpour, H. & Vinuesa, R. 2021 From coarse wall measurements to turbulent velocity fields through deep learning. *Phys. Fluids* **33** (7), 075121.
- He, K., Zhang, X., Ren, S. & Sun, J. 2016 Deep residual learning for image recognition. In *2016 IEEE Conf. Comp. Vision and Pattern Recogn. (CVPR)*, pp. 770–778.
- Kim, J. & Lee, C. 2020 Prediction of turbulent heat transfer using convolutional neural networks. *J. Fluid Mech.* **882**, A18.
- Kingma, D. P. & Ba, J. 2015 Adam: A method for stochastic optimization. In *3rd Int. Conf. on Learning Representations, ICLR 2015, San Diego, CA, USA, May 7-9, 2015*.
- Quadrio, M., Ricco, P. & Viotti, C. 2009 Streamwise-travelling waves of spanwise wall velocity for turbulent drag reduction. *J. Fluid Mech.* **627**, 161–178.
- Raiola, M., Greco, C. S., Contino, M., Discetti, S. & Ianiro, A. 2017 Towards enabling time-resolved measurements of turbulent convective heat transfer maps with ir thermography and a heated thin foil. *Int. J. Heat Mass Trans.* **108**, 199–209.
- Ronneberger, O., Fischer, P. & Brox, T. 2015 U-net: Convolutional networks for biomedical image segmentation. pp. 234–241. Springer.
- Sasaki, K., Vinuesa, R., Cavalieri, A. V. G., Schlatter, P. & Henningson, D. S. 2019 Transfer functions for flow predictions in wall-bounded turbulence. *J. Fluid Mech.* **864**, 708–745.
- Tomiyama, N. & Fukagata, K. 2013 DNS of drag reduction in a turbulent channel flow using spanwise traveling wave-like wall deformation. *Phys. Fluids* **25** (10), 105115.

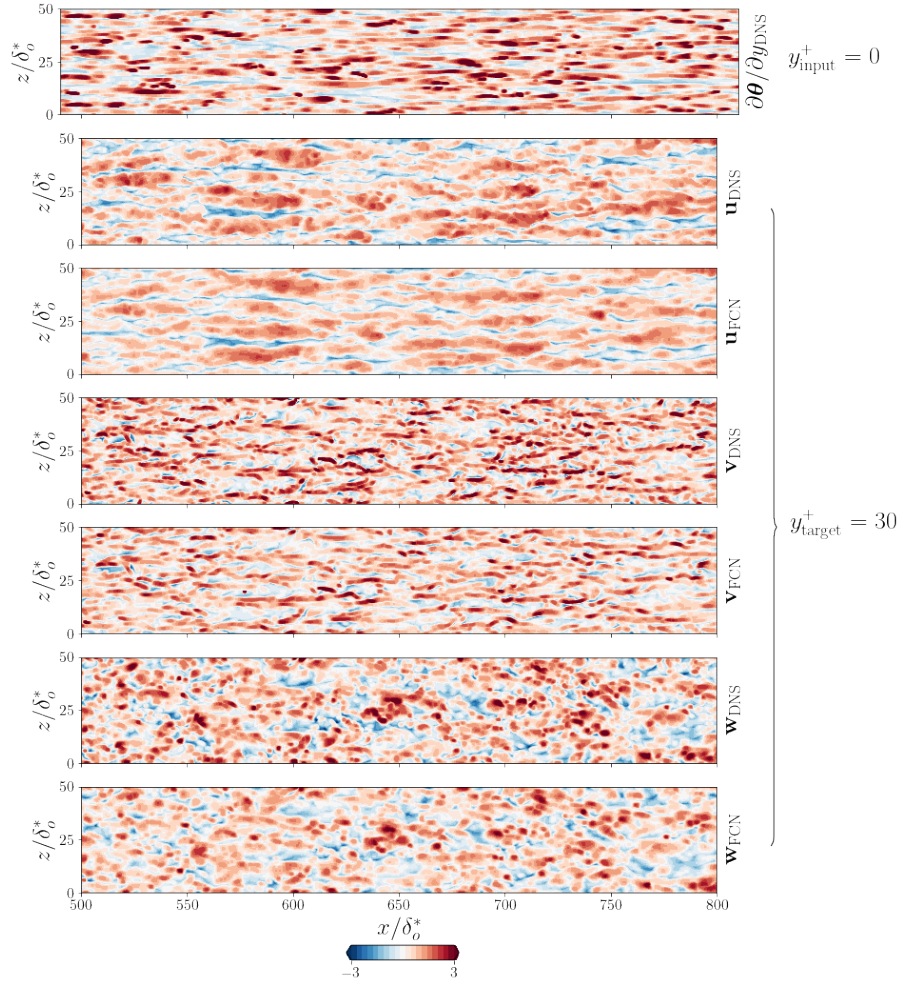


Figure 4. Sample result for *type-III* prediction at $y^+ = 30$, obtained using the proposed FCN with auxiliary loss functions. The first row corresponds to the DNS input heat flux for $Pr = 6$, normalized with the mean and standard deviation computed on the training samples. The second and third rows show the streamwise DNS velocity-fluctuation field and the corresponding prediction obtained from FCN, respectively. Similarly, the fourth and fifth rows represent the wall-normal velocity fluctuation of the target and predicted fields. Finally, the sixth and seventh rows show the spanwise velocity fluctuation component of the target and predicted fields, respectively. The velocity-fluctuation fields are scaled by the respective RMS quantities.

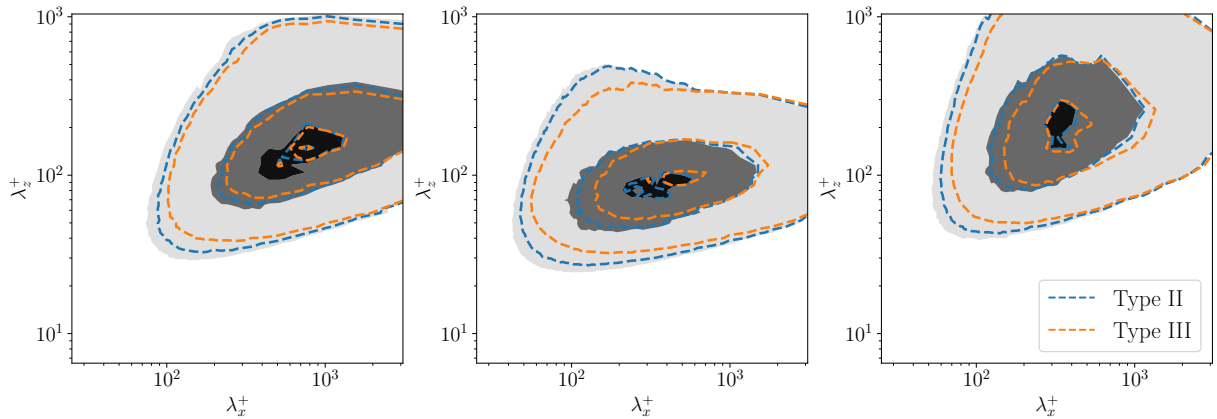


Figure 5. Pre-multiplied two-dimensional power-spectral densities. The three rows represent $k_z k_x \phi_{uu}$ (left), $k_z k_x \phi_{vv}$ (center), $k_z k_x \phi_{ww}$ (right). The contour levels contain 10%, 50% and 90% of the maximum DNS power-spectral density. Shaded contours refer to the reference data, while contour lines refer to *type-II* (blue) and *type-III* (orange) predictions, respectively.